E14-2002-161

Yu. V. Taran, M. R. Daymond[1], D. Eifler[2], Th. Nebel[2],
J. Schreiber[3]

STUDY OF MECHANICAL FEATURES FOR LOW CYCLE FATIGUE SAMPLES OF METASTABLE AUSTENITIC STEEL **AISI 321** BY NEUTRON STRESS ANALYSIS UNDER APPLIED LOAD

[1]ISIS, Rutherford Appleton Laboratory, Chilton, Oxon OX11 0QX, UK
[2]DMS, University of Kaiserslautern, D-67653 Kaiserslautern, Germany
[3]EADQ, Fraunhofer Institute for Nondestructive Testing,
D-01326 Dresden, Germany

1. Background

Austenitic stainless steels (ASS) are widely used in engineering applications because of their high corrosion resistance and toughness. A major concern in a number of applications including nuclear power plants, however, is fatigue damage of ASS components. During fatigue loading microstructural changes occur in ASS which affect both the mechanical and physical properties of the steel. The ferromagnetic martensitic phase formed in some ASS due to the plastic deformation occurring during mechanical fatigue presents a particularly interesting phenomenon. In these materials a metastable austenitic *fcc* structure twists into a martensite tetragonal distorted lattice, i.e. the austenite is converted directly, or indirectly over the hexagonal paramagnetic ε-martensite, into the ferromagnetic α′-martensite. The extent of distortion depends strongly on the carbon content. For low carbon steels the tetragonal structure does not deviate much from the *bcc* lattice of α-Fe. When induced by plastic deformation, the martensitic phase usually first forms at faults in the initial austenitic matrix such as carbides, stacking faults, twins, etc., in the form of needles or lathes and later as blocks or bands. As a result, texture or preferred orientation in the growing martensitic phase often accompanies this kind of phase transformation. Many investigations have shown the influence of the martensitic transformation on the fatigue properties of ASS (see, e.g., [1]). Whereas the mechanical properties of austenitic steel are well known [2], a transforming or partly transformed material is much more difficult to characterise due to the interaction between two phases. For instance, the elastic mismatch and the plastic misfit between the martensite and austenite, as well as the larger specific volume of martensite are likely to cause considerable stresses throughout the sample. A knowledge of the residual stress state of the phases and their relation to the fatigue process is very important, in order to develop a proper understanding of how the individual phases interact to produce the bulk mechanical response of the material.

At present perhaps the most comprehensive stress measurements with neutron diffraction can be performed on dedicated time-of-flight diffractometers at pulsed sources equipped with modern strain scanners and appropriate loading machines. Such installations provide unique possibilities to study the mechanical behaviour of the individual phases in a multiphase material. The ENGIN instrument [3] at the ISIS neutron pulsed facility has excellent parameters and sample-environment equipment for such research.

This paper describes in detail a study of a low carbon metastable austenitic stainless steel of type AISI 321 with varying martensite volume fractions produced by plastic deformation during low cycle fatigue. The work was published previously in brief [4]. Information about the mechanical properties of the bulk samples, of the austenitic matrix and of the martensitic phase have been obtained from the experimental mechanical and neutron diffraction data.

Section two of the paper gives information about the material and the samples used for cycling and monotonic testing. In section three, the experimental set-up is described along with the procedure for processing the time-of-flight neutron diffraction spectra. Section four contains the results of the experimental determination of lattice parameters, the elastic strains, the elastic constants, the martensite fractions, the texture index, the residual and anisotropy strains and residual stresses, which are then discussed in section five before concluding in section six.

2. Material and Samples

The material examined in this work was a low carbon Ti-alloyed austenitic stainless steel X6CrNiTi1810 with the major components 17.74 % Cr and 9.3 % Ni (German-grade 1.4541, which is an analogue of the US-grade AISI 321). The steel was delivered as a cold formed bar with a diameter of 20 mm. The yield stress $R_{p0.2}$ and the tensile strength R_m were 192 and 580 MPa, respectively. The bars were annealed at 1050 °C and quenched in water. A set of eight samples (Table 1) were machined from these bars. The central gauge of the sample (Fig. 1) had a diameter of 7.5 mm

and a length of 16 mm. The fatigue loading at DMS was performed on a MTS 100 kN servohydraulic testing machine at room temperature. Seven of the eight samples (A to G in Table 1) were cycled under uniaxial tensile-compressive loading under total-strain control with a triangular waveform and an amplitude of 1% (a strain ratio R_ε=-1) at a frequency of 0.5 Hz. While sample A was cycled to failure, six of them (B to G) were each subjected to varying numbers of fatigue cycles. The variation of the maximum stress amplitude (MSA) for these samples is also shown in Table 1.

In all cases, the fatigue experiment was stopped after a compressive half cycle, therefore the residual macroscopic plastic strain (RPS) was negative in all the unfractured samples (Table 1). Sample B was cycled up to about 90 % of the fracture fatigue level determined from Sample A. A macro-crack in sample B was observed after the subsequent tensile loading of the neutron experiment (Fig. 1). It is possible that the unusual behaviour of this sample, which will be discussed below, but for example includes the dependence of the anisotropy strain on the applied stress, was caused by this crack which could act to relax the residual stresses accumulated during fatigue cycling. Sample H, which was not cycled, provides a reference sample for the austenitic phase.

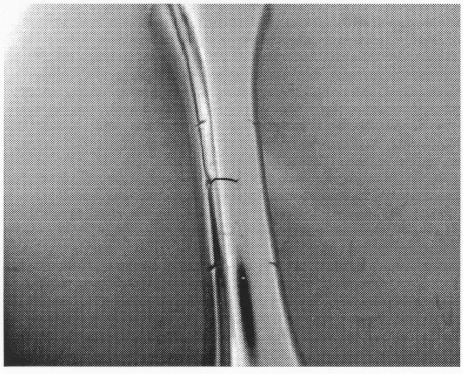

Fig. 1. View of sample B (the macro-crack is found after the neutron experiment).

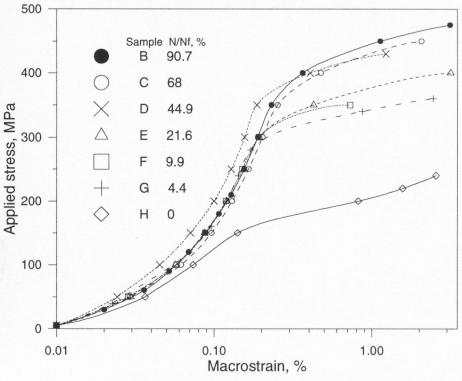

Fig. 2. Applied stress-bulk macrostrain responses of the LCF-samples.

Table 1. LCF-samples: Mechanical data.

Sample	N	N/N_f, %	MSA, MPa	RPS, %	E_{bulk}, GPa*	E_{bulk}, GPa***
A	1161	100	452.9	-0.627		-
B	1053	90.7	472.8	-0.672	171(23)	-
C	789	68.0	453.58	-0.689	148(5)	194.7(2.8)
D	521	44.9	426.2	-0.714	183(6)**	179.5(2.4)
E	251	21.6	392.4	-0.744	164(9)	182.2(2.2)
F	115	9.9	373.9	-0.759	165(5)	177.5(2.2)
G	51	4.4	363.8	-0.766	163(16)	179.1(2.6)
H	0	0	-	-	151(14)	186.5(1.5)

** In-situ tensile measurements during the neutron experiment.*

*** Corrected on the extensometer slip.*

**** Measurements after the neutron experiment by help of the specialised equipment of DMS.*

During the neutron measurements the macrostrain in the axial direction was recorded using a clip gauge extensometer. In Fig. 2, the applied stress-bulk macrostrain response is shown for all samples. The macroscopic Young's modulus E_{bulk} (i.e. the elastic slope of the bulk stress-strain response) obtained by linear fit of the initial part of the curve is presented in Table 1. However during

the processing of the bulk measurements we observed that the knife blades of the extensometer occasionally showed some slip on the surface of the sample before settling in. Thus, there is some uncertainty in the strain change at low loads. Therefore we have repeated the bulk measurements of Young's modulus after the neutron experiment on the specialised equipment of DMS. To stabilise the extensometer knifes on the sample surface, four tensile-compressive cycles were first performed with an amplitude of 3.5 kN at a rate of 1.5 kN/s. The beginning linear part of the fifth loop from 0 to 20 MPa is used to determine the slope from which the bulk Young's modulus presented in Table 1 is calculated.

The samples were tested to determine the martensite volume fraction 'f' before and after the neutron experiment with help of a commercial FerriteScope device based on the magnetic inductive method. Results of these measurements will be discussed together with the neutron data below.

3. Set-up of the Experiment and Processing of the Diffraction Spectra

The samples were measured using the *in situ* Instron servohydraulic stress rig under tensile stress control on the ENGIN instrument. The stress rig loading axis is horizontal at 45° to the incident neutron beam, thus providing simultaneous measurements of strains parallel (axial) and perpendicular (transverse) to the applied stress [5]. A neutron gauge volume of $\approx$50 mm^3 is formed inside the central part of the sample in a form of the thin rectangular parallelepiped, located at 45° to the sample axis, with thickness of 2 mm and the incident dimensions of 5×5 mm^2 by using two multislit radial collimators in front of the ±90° detectors and a primary slit in front of the sample, respectively.

The collected detector counts are treated to provide a diffraction pattern of intensity versus neutron time of flight or crystalline lattice spacing. The calibration of the detectors was performed by using a Si standard powder sample from NBS (USA). The result of the calibration is an instrument parameter file which holds the geometric description of the instrument, characteristic intensity spectrum and other specific data (e.g. [6]). Processing of the Si-spectra (Fig. 3) using the parameter file obtained gave the following lattice parameters: 1) a_{ax}=5.430995(48) Å for the right (+90°) detector, and 2) a_{tr}=5.430970(50) Å for the left (-90°) detector. Characterising the symmetry of the detectors by the pseudostrain $\varepsilon=0.5(a_{ax}-a_{tr})/(a_{ax}+a_{tr})$ and using a typical value of Young's modulus equal to 200 GPa we obtain a nominal detector asymmetry error in the determination of the stress of 1 MPa, assuming that the gauge volume remains submerged, or in the case of a gauge larger than the sample that the sample remains centred.

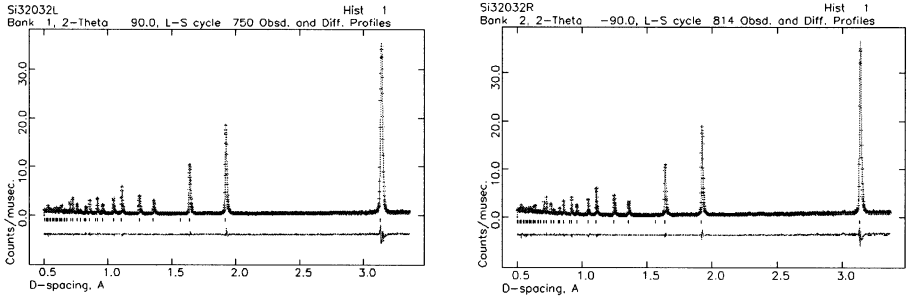

Fig. 3. Diffraction spectrum of the Si standard powder sample: left - the transverse direction, right - axial direction. The crosses show the measured data and the line connecting them is the Rietveld fit. The tick marks show the peak positions. The lower graph is the difference curve (to the same scale as the data).

The lattice parameters of the austenitic and martensitic phases were determined using both Rietveld and Le Bail refinements (RR/LBR) implemented within the GSAS software package [7]. Fitting was carried out in a d-spacing interval from 0.04 to 0.23 nm in which 38 austenite and 32 martensite reflections are observed. An example of LBR is shown in Fig. 4 for sample B.

We performed a test using both refinement methods on the same spectra and obtained coincident results for lattice parameter within experimental errors. In LBR, a structure-free approach is used, i.e. the intensities of the reflections are simply adjusted to fit the observed ones. Therefore LBR does not give a possibility to determinate the martensite fraction and the texture index. For this we used RR with the spherical harmonic model that can be chosen within the GSAS code [7].

The strains within individual grain families of both phases are determined by single peak fitting of individual reflections using the RAWPLOT subroutine in the GSAS code.

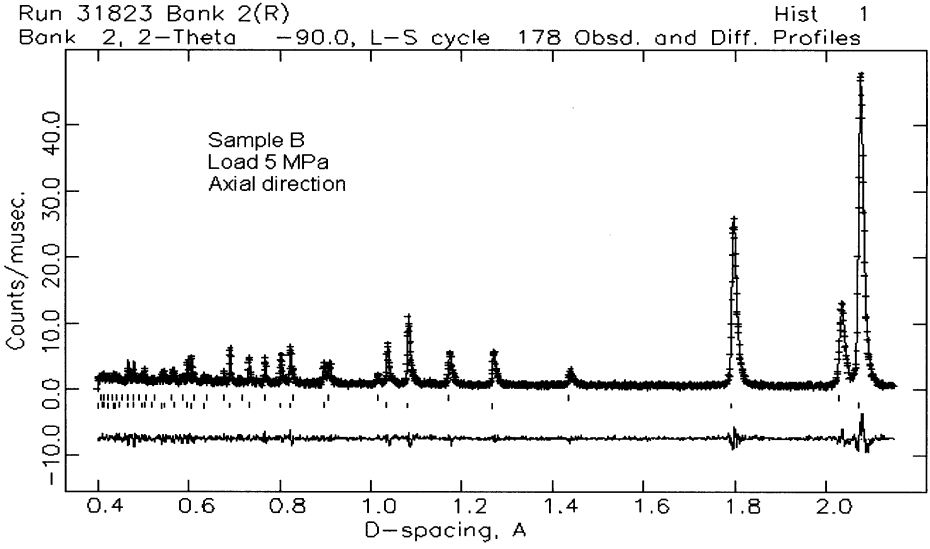

Fig. 4. Diffraction spectrum for the sample B (martensite fraction 25 Vol. %) under 5 MPa tensile load in the axial direction. The crosses show the measured data and the line connecting them is the Le Bail fit. The tick marks show the peak positions: top - martensite, below - austenite. The lower graph is the difference curve (to the same scale as the data).

The conventional refinement that we use to obtain elastic lattice parameter strain does not account for the elastic anisotropy of various crystal planes under loading. For a small uniaxial load the refinement produces a good fit as illustrated in Fig. 5 (left) for example of sample H (austenite only). For a higher applied load the difference curve demonstrates shifts of the (111) and (200) peaks in the opposite directions relative to those obtained with an isotropic model used in the conventional fit shown in Fig. 5 (centre). Note that the (111) and (200) planes represent the extremes of elastic stiffness in cubic materials. Following [2] we reprocessed the entire experimental data using the modified LBR accounting for elastic anisotropy, and calculated the anisotropy strains. The fitting results for sample H are shown in Fig. 5 (right). In this case, the quality of the fit is strongly improved.

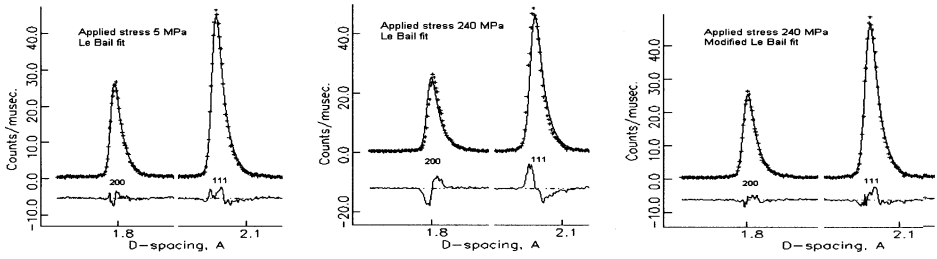

Fig. 5. Part of the spectrum for the sample H (austenite) in the axial direction: left - under 5 MPa tensile load, centre and right - under 240 MPa. The crosses show the measured data and the line through them is the result of: left and centre - the conventional Le Bail fit, right - the modified Le Bail fit.

4. Experimental Results

4.1. Lattice parameters. The direct result from processing the neutron diffraction data is the dependence of the phase lattice parameter a_{ii} on the applied stress σ_L for directions 'ii' equal to '11' or '33', corresponding to the axial or transverse direction, respectively. An example of the lattice parameter dependencies of austenite and martensite are shown for sample B in Fig. 6.

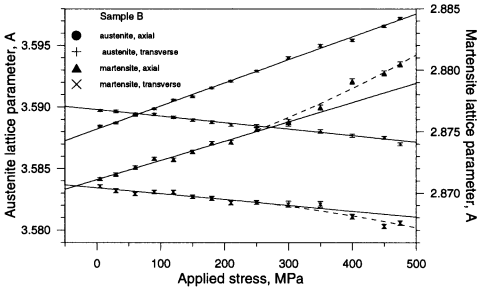

Fig. 6. Lattice parameters of austenite and martensite vs applied stress for the sample B.

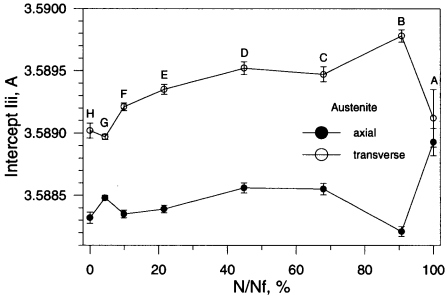

Fig. 7. Intercepts I_{11} (black points) and I_{33} (open points) of austenite vs fatigue level, obtained from figures comparable to Fig. 6.

In the Appendix we will show that from the linear fit of the elastic part of the phase curves $a_{ii}(\sigma_L)$ it is possible to obtain the intercepts I_{11} and I_{33} (Figs. 7 and 8), the slopes S_{11} and S_{33} which depend on the phase elastic constants E and ν, the stress-free value of the phase lattice parameter a_0 and the total phase stress tensor. The calculation of these latter values is the main goal of the following discussion.

4.2. Elastic strains. A rough approximation for calculating elastic strains $\varepsilon_{ii}=(a_{ii}-I_{ii})/I_{ii}$ is to use the intercepts I_{ii} instead of the stress-free value of the phase lattice parameter a_0. In this case we ignore the residual stresses created during fatigue cycling, characterising the relative changes in the sample during loading. The applied stress - elastic strain responses of individual phases obtained using this approximation is shown for sample B in Fig. 9.

While the martensite strain deviates from linearity quite significantly in the bulk plastic regime, the austenite strain shows very little deviation. In fact this behaviour was observed in general in the samples. Any deviation from linearity in the austenite response was much smaller than that seen in the martensite, and moreover, extremely small compared to that expected based on simple load

sharing arguments, given the large volume fraction ' f ' of martensite (for sample B, $f \approx 25$ vol.%). A correlation with the onset of the deviation of the martensite strain from linearity with the macroscopic yield stress $R_{p0.2}$ was observed.

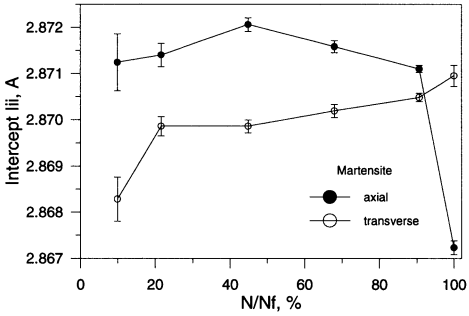

Fig. 8. Intercepts I_{11} (black points) and I_{33} (open points) of martensite vs fatigue level, obtained from figures like Fig. 6.

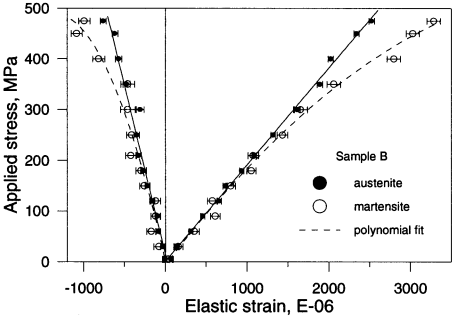

Fig. 9. Applied stress - elastic strain responses of the individual phases in sample B.

4.3. Elastic constants. The phase lattice parameter measured for a single diffraction peak is along a particular crystallographic direction that has its own elastic constants. In general the neutron elastic constants will differ from the bulk elastic constants and will depend on preferred orientations of crystallines, i.e. the texture of the material. However, as shown in [2] for a randomly textured single phase ASS, the lattice parameter obtained from a Rietveld/Le Bail multi-peak refinement provides elastic constants close to the bulk macroscopic values. A rigorous approach to determining elastic constants in the presence of applied stress is given in the Appendix, where we have introduced so-called "quasielastic" constants $E_{ax}=I_{11}/S_{11}$ and $E_{tr}=I_{33}/S_{33}$ for the axial and transverse directions, respectively. The calculated "quasielastic" constants for both directions, as well as the ratio of E_{ax}/E_{tr} are presented in Figs. 10 and 11. Only in the absence of the residual stresses the "quasielastic constants " E_{ax} and E_{tr} turn into the true elastic constants E and -E/ν, respectively. However, for typical values of stress and modulus the effect of the residual stress state on the observed modulus will be very small; typically ≤ 0.1%. Note that both of the austenite elastic constants in Figure 10 increase slowly with fatigue level, for values of $N/N_f \geq 10\%$.

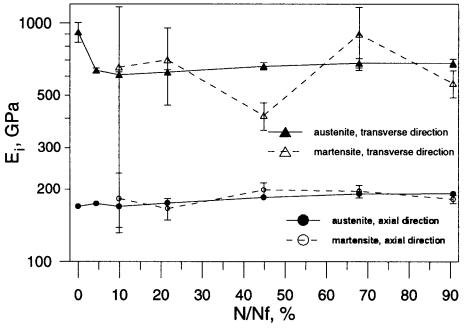

Fig. 10. "Quasielastic" constants E_i (here i='ax' or 'tr') of austenite and martensite vs fatigue level.

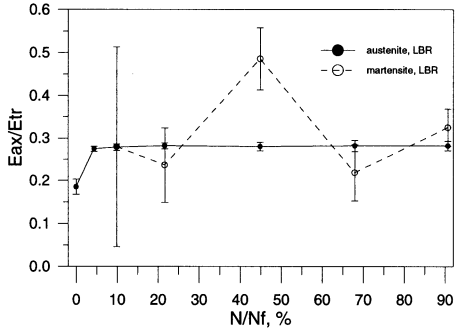

Fig. 11. Ratio of "quasielastic" constants E_{ax}/E_{tr} for austenite and martensite vs fatigue level.

The ratio E_{ax}/E_{tr} should be equal to Poisson's ratio ν assuming macroscopic isotropy of the material and an absence of residual stresses. In both austenitic and martensitic steels, macroscopic Poisson's ratio of about 0.28–0.3 are typical [8]. It is remarkable that the ratio of E_{ax}/E_{tr} (Fig. 11) are very close to this value, in spite of the strong scatter of the experimental points observed for the martensite phase in the transverse direction.

Note that the pure austenite sample H drops below the common line: its ratio of E_{ax}/E_{tr}=0.185(18) is appreciably lower than the austenite phase ratio of the other samples (Fig. 11). On the other hand as is shown in the Appendix (Eq.(A13)) in the case of the single phase system Poisson's ratio may be exactly determined from the linear fits of the experimental curves $a_{11}(\sigma_L)$ and $a_{33}(\sigma_L)$ even if residual stresses are present in the sample. We shall return once more to the problem of determining neutron elastic constants below.

4.4. Martensite fraction. The martensite volume fraction '*f*' measured without load and at the maximum value of the applied stress are presented in Table 2 for both axial and transverse directions. In the same table the results of the martensite fraction determination using the FerriteScope before and after the neutron experiment are shown too. The variation of martensite volume fraction under applied stress is shown in Fig. 12. Note that the onset of the increase in the martensite volume fraction occurs at levels of the applied stress considerably larger than the yield stress $R_{p0.2}$ of the uncycled austenite steel.

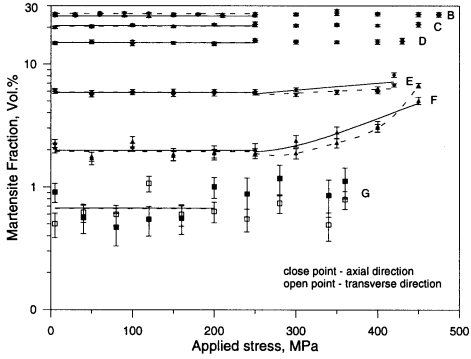

Fig. 12. Martensite fraction vs the applied stress.

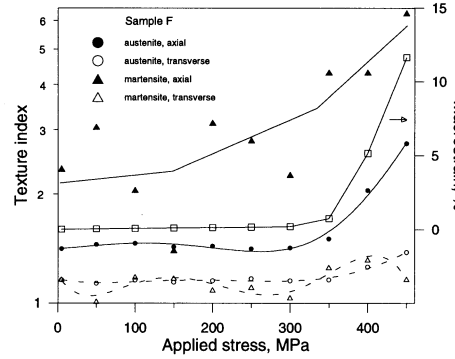

Fig. 13. Texture index in the sample F vs the applied stress as well as macrostrain.

Table 2. Martensite fraction and texture data.

Sample	"neutron" *f*, vol. % (ax/tran)		"magnetic" *f*, vol. %		Texture index (ax/tran)	
	without load	max load	before	after	austenite	martensite
A	25.2(5)/24.1(7)		48	23.5	1.31/1.11	1.25/1.15
B	24.8(2)/25.9(3)	25.5 (only ax)	41	18.3	1.61/1.25	1.12/1.02
C	20.7(6)/20.5(4)	21.1	31	16.5	1.41/1.10	1.26/1.01
D	14.9(6)/15.1(2)	15.5	22	14.8	1.52/1.04	1.19/1.04
E	5.9(2)/5.9(2)	7.5	10.3	6.0	1.42/1.16	1.41/1.08
F	2.0(2)/2.0(2)	5.9	4.1	9.5	1.43/1.15	2.46/1.12
G	0.68(22)/0.67(20)	0.96	2.3	2.2	1.52/1.40	12.5/4.1
H					1.46/1.16	

4.5. Texture. The texture index was determined using a spherical harmonics approach within the Rietveld refinement. The sample symmetry was chosen as a cylindrical fibre texture. A satisfactory agreement with the measured diffraction spectra was obtained with two spherical harmonic terms. The magnitude of the texture can be characterised by the texture index J. If the texture is random then J=1, otherwise J>1; for a single crystal J=∞. The phase texture index (without the load) in both axial and transverse directions are shown in Table 2. In considering both the martensite volume fraction results and the texture results it should be noted that since we are obtaining both texture and volume fractions from only two diffraction spectra, the uncertainty on the results will be quite high and we should seek to observe only general trends. Nonetheless it was observed that the texture index of the austenite in the axial direction show a slight increase with increasing fatigue level while in the transverse direction it is almost constant. In the martensite phase the texture index decreases in both directions with increasing fatigue. The only strong texture observed is in the martensite at low volume fractions, which corresponds to the initial transformation of only the most preferentially oriented austenite crystallites. The texture for low martensite volume fraction was shown particularly clearly in the martensite 110 peak which was relatively strong parallel to the fatigue loading axis. The texture index of both the austenite and martensite in the axial direction increased during the neutron loading test at high plastic strains (in Fig. 13, the results from sample F is shown as an example, where the texture starts to increase at a macroscopic strain of about 2%).

4.6. Residual Strain. In order to trace the evolution of residual strains in the austenitic phase with fatigue level, the initial austenite residual strain in each direction was calculated, using the lattice parameter $a_{aus}(\sigma_L=0)$ in the initial unloaded state, i.e. the value of the intercept I_{11} or I_{33} (see Eqs.(A21-A22)), compared to the equivalent parameter of sample H in the same direction as a "stress-free" value. Thus, we ignore any residual stress created in sample H during quenching. In this case, it is found that the austenitic matrix showed a weak expansion in lattice parameter as a function of cycling (Fig. 14). We can only apply this approach to austenite, since no suitable martensite reference exists.

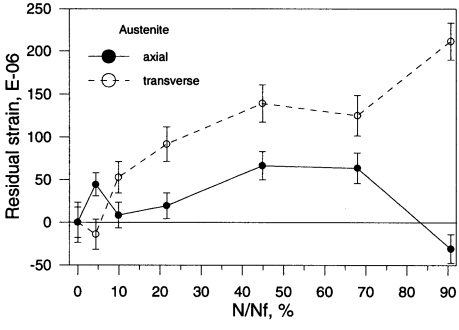

Fig. 14. Residual strains in the austenite vs the fatigue level.

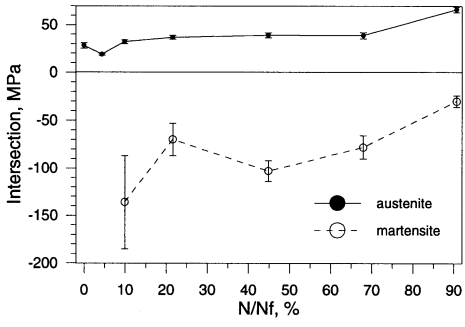

Fig. 15. Intersection σ_L^* for austenite and martensite vs fatigue level.

4.7. Residual Stress. To calculate the phase residual stress from the experimental data the stress-free phase lattice parameter a_0 has to be known. Usually in order to determine this parameter a sample is made with the same structure, but free from internal stresses. However, in our case such samples were not available. As shown in the Appendix, the *deviatoric* components of the residual stress tensor may be determined without the accurate knowledge of the stress-free phase lattice parameter a_0 (see also [9]). While it is desirable to know the entire residual stress tensor the deviatoric residual stress tensor will be sufficient to track the change of the residual stresses during LCF-testing.

First of all consider results from the neutron experiment with sample H, as this sample represents the single phase system (austenite) and, hence, is easier to interpret. In this case any microstresses σ_{ij}^{m} (e.g. elastic incompatibility (mismatch) stresses) induced by the applied stresses are not present. Using Eq.(A19) from the Appendix and the intersection σ_L^* from Fig. 15 we obtain the deviatoric residual stresses τ_{11}^R=-14.0(1.5) MPa and τ_{33}^R=14.0(1.5) MPa, i.e. a small compressive stress in the axial direction and a small tensile stress in the transverse direction, respectively.

Concerning the origin of observed stresses in sample H, we must first note that the neutron gauge volume was fully submerged in the sample, and thus did not fully bathe a cross section of the sample. A sample subjected to very strong cooling during quenching (in our case in water) will experience plastic flow and hence a residual stress state due to the high thermal gradients. During the quenching some parts of the samples can reach the yield stress and consequently undergo significant plastic strains resulting in residual stress fields which vary from compressive close to the sample surface to tension in the centre. In this case the quenching residual stresses can have both hydrostatic and deviatoric components. Since this sample was machined down from 20 to 7.5 mm in diameter subsequent to the quench, we would expect very little thermal stress in the transverse direction, which the experimental value of τ_{33}^R seems to confirm.

To calculate the deviatoric phase residual stresses in the other samples which contain both austenite and martensite phases (see Eq.(A34)) we have neglected the phase microstresses σ_{ij}^{m} induced by the applied stress since, as seen in Fig. 10, the elastic properties of both phases are similar (see also Section 5), and consequently, any microstresses due to differences in the elastic behaviour of the two phases are small compared to those due to the different plastic behaviour (see Fig. 9). The deviatoric phase residual stresses calculated as shown in the Appendix are presented in Fig. 16.

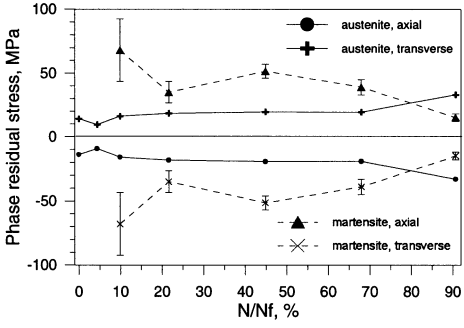

Fig. 16. Deviatoric phase residual stresses in austenite and martensite vs the fatigue level.

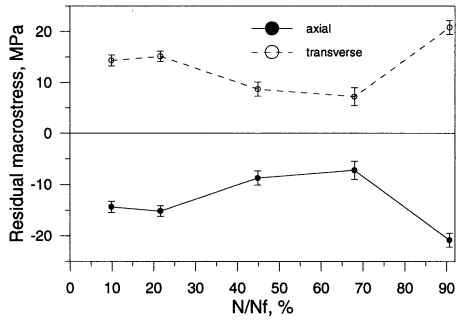

Fig. 17. Deviatoric residual macrostresses vs the fatigue level.

The deviatoric residual stresses in all the samples have been separated into the austenite and martensite contributions. The austenite deviatoric residual stress is compressive in the axial direction and tensile in the transverse direction. At the same time the martensite deviatoric residual stress in the same directions have the opposite sign and their values are larger then in the austenite matrix in accordance with the smaller volume fraction. The large martensite residual stress could lead to the crack initiation that was observed in sample B at 90 % fracture fatigue level.

According to Eq.(A35) the total deviatoric residual stresses in each phase, ${}^{a}\tau_{ii}^R$ and ${}^{m}\tau_{ii}^R$, where the index 'a' and 'm' are for austenite and martensite, respectively, may be separated into the macrostresses τ_{ii}^M (Fig. 17) and the microstresses in each phase, ${}^{a}\tau_{ii}^{\mu}$ and ${}^{m}\tau_{ii}^{\mu}$ (Fig. 18). The deviatoric residual macrostress in all the samples shows a compressive axial component and a tensile transverse component. The austenite microstress is tensile in the axial direction and compressive in the

transverse direction, while the martensite microstresses are of correspondingly opposite sign, with magnitudes larger then in the austenite matrix in accordance with the smaller volume fraction.

If an entire sample cross section were irradiated in the neutron beam, the average residual macrostress must be zero and only the residual microstresses can be measured. If we made this assumption, it would follow from Eq.(A37) that we can also calculate the hydrostatic macrostress τ_H^M and thereby restore the total residual macrostress tensor σ_{ii}^M, i.e. in this case the axial component σ_{11}^M while the transverse components σ_{33}^M =0 due to Eq.(A36). The axial component of the total residual macrostresses is compressive that correlates with the negative residual plastic strain after the fatigue cycling. If we do carry out this analysis, recognising its inherent inaccuracy, we obtain the results shown in Fig 19. The fact that of the axial component of the residual macrostress tensor is not equal to zero indicates the incomplete averaging of the residual macrostresses in the neutron gauge volume.

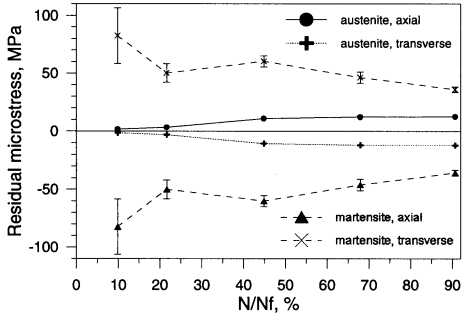

Fig. 18. Deviatoric residual microstresses in austenite and martensite vs the fatigue level.

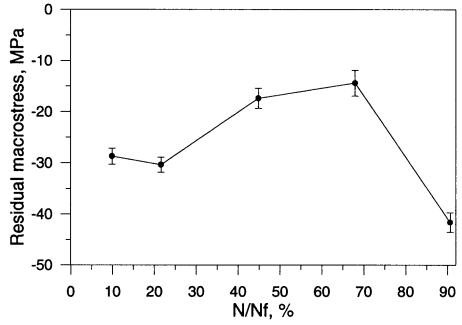

Fig. 19. Axial residual macrostresses vs the fatigue level.

4.8. Strain vs Anisotropy Factor. Single peak analysis using GSAS was carried out for many reflections of both the austenitic and martensitic phases. It was observed that the elastic strains of both phases vary linearly with the anisotropy factor $G=(h^2k^2+h^2l^2+k^2l^2)/(h^2+k^2+l^2)$ up to a stress of 400 - 500 MPa (Figs. 20 and 21). According to Pintschouvius's criterion [10] this indicates that the measured elastic strains are of type I.

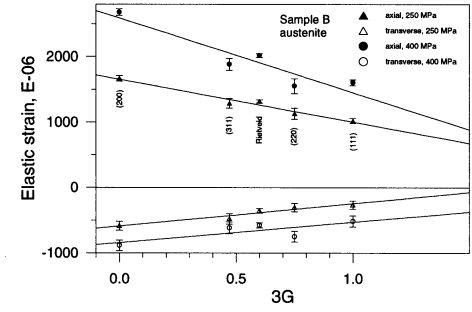

Fig. 20. Elastic strain in the austenite phase of sample B vs the anisotropy factor G for an applied stress 250 and 400 MPa, respectively.

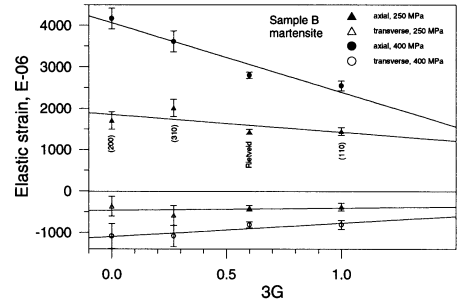

Fig. 21. Elastic strain in the martensite phase of sample B vs the anisotropy factor G for an applied stress 250 and 400 MPa, respectively.

4.9. Anisotropy Strain. The results of the modified LBR are: 1) the determination of the value of the lattice parameter which tracks a nominal *h00* direction and thus the elastic strains ε_{h00} for (*h00*) reflections can be calculated, 2) the determination of a new fitting parameter ε_A (the so-called anisotropy strain) which shifts the position of each peak from perfect cubic structure by a value proportional to the anisotropy factor G. Concerning the anisotropy strain in the austenite phase the results obtained for a majority of the samples are close to those reported in [2] (Fig. 22 illustrates the results for sample D). Note that the initial anisotropy strain observed is non zero in the fatigued samples due to plasticity induced intergranular strains.

We have also observed the division of the anisotropy strain into two components (the example is shown in Fig. 23 for sample D). However we have not observed the relatively sharp change in slope in the dependence of the austenite anisotropy strain with the elastic strain. Instead the transition from the elastic component to the plastic component takes place fairly smoothly. Note that the transition region correlates with the onset of macroscopic plasticity (see the macrostrain response in Fig. 22). The influence of the fatigue level on the anisotropy strain is presented in Fig. 24 (note the unusual behaviour of the anisotropy strain in sample B). For reasons of legibility, the experimental points are left out, and only the results of the second degree polynomial fit (excluding the sample B with a third degree polynomial fit) are shown.

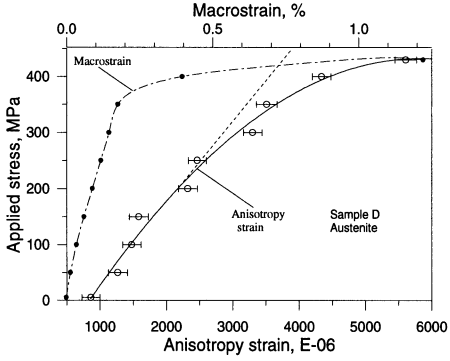

Fig. 22. Austenite anisotropy strain response (sample D) and the stress-macrostrain response.

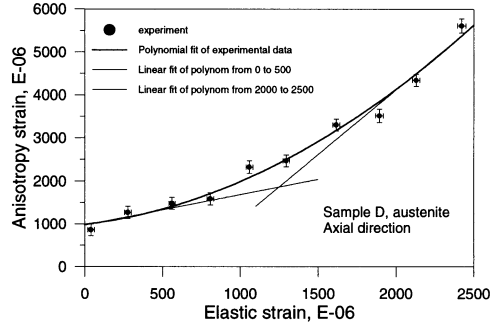

Fig. 23. Variation of the austenite anisotropy strain with the elastic strain as determined by the Le Bail fit for the sample D.

The elastic hkl-strains of the austenite phase can be calculated from the modified LBR results by the formula

$$\varepsilon_{hkl} = \varepsilon_{h00} - \varepsilon_A G \qquad (1)$$

and these can be compared with the results of the single peak analysis. The results of the both determinations of the austenite elastic strain response in the axial direction of the (111), (200), (220) and (311) planes coincide with each other semi-quantitatively even for the sample B (Fig. 25).

A different picture is observed for the martensite phase. Though there is a qualitative similarity between the applied stress - anisotropy strain response in the austenite and martensite phases, the division of the martensite anisotropy strain into two components strongly depends on the fatigue level (Fig. 26). For example, in the samples with small martensite fraction the dependence of the martensite anisotropy strain on the martensite elastic strain is practically linear. The elastic anisotropy hkl-strains of the martensite phase agree semi-quantitatively with results of single peak analysis of of the (110), (200) and (310) reflections (Fig. 27).

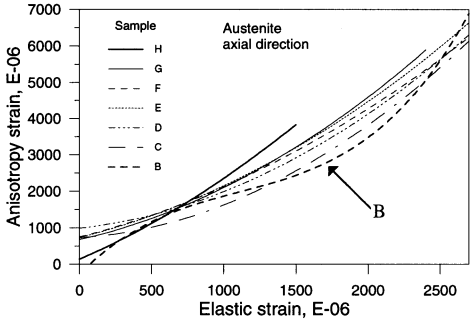

Fig. 24. Variation of the austenite anisotropy strain with the elastic strain for the LCF-samples. An arrow indicates the B line.

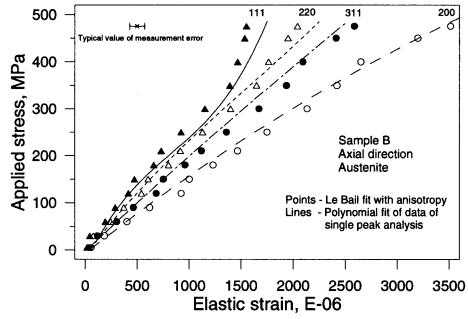

Fig. 25. Austenite strain response in the axial direction of the individual planes: points - calculated from modified the Le Bail fit, lines - determined by single peak analysis.

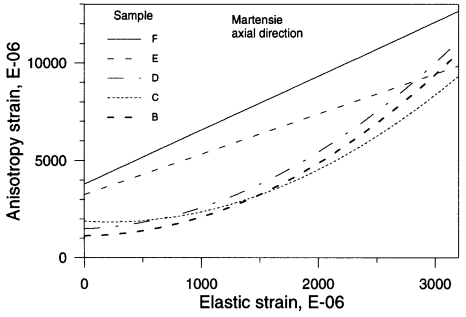

Fig. 26. Variation of the martensite anisotropy strain with the elastic strain as determined by the Le Bail fit for all the low cycle fatigued samples.

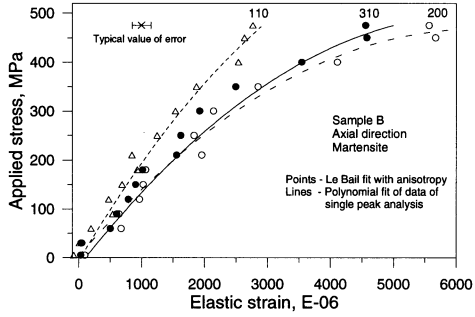

Fig. 27. Martensite strain response in the axial direction of the individual planes: points - calculated from modified the Le Bail fit, lines - determined by single peak analysis.

5. Discussion

5.1. Elastic constants and residual stresses. The mechanical properties of two phase materials depend on the properties of the individual phases and their interactions within the material. In the samples studied we have seen (Fig. 10) that the austenite and martensite "quasielastic" constants are similar. This gives us the basis to neglect entirely the elastic phase microstress induced by the applied stress during the calculation of the residual macrostresses and the phase deviatoric residual microstresses. Similarly we calculate the phase elastic constants using Eqs.(A26-A27). In this case the ratio of slopes S_{11}/S_{33} (see Eq.(A26)) yields phase Poisson's ratio ν. From Eq.(A27) we can obtain the difference between the phase axial "quasielastic" constant and the true phase Young's modulus:

$$E_{ax} - E = (1-2\nu)\tau_H^I - \frac{2}{3}(1+\nu)\sigma_L^* \ . \qquad (2)$$

To estimate the difference shown on the left hand side of Eq.(2) we have to know the phase hydrostatic residual stress τ_H^I. Yet a true value cannot be obtained without knowledge of an accurate value of the stress-free phase lattice parameter. Nevertheless we shall try to understand the extent to

which the hydrostatic residual stress can influence Eq.(2) by changing the hydrostatic value, for example, between limits from 0 up to 200 MPa. As can be seen from Fig. 28 this influence is very small, as expected less than 0.1% in the worst case, i.e. less than the experimental errors in the determination of the phase "quasielastic" constants, giving further confidence that the "quasielastic" constants can be used as equivalent to the true values.

Another approach to estimating the influence of the residual stresses on the determination of the elastic constants consists in a study of the difference of the elastic strains in the axial and transverse directions vs the applied stress. From Eq.(A5) we obtain

$$\varepsilon_{11} - \varepsilon_{33} = \frac{1+\nu}{E}\sigma_L + \frac{1+\nu}{E}(\sigma_{11}^R - \sigma_{33}^R). \qquad (3)$$

To calculate the strain we exchange a stress-free reference lattice parameter a_0 with the average value of $(I_{11}+I_{33})/2$ where the intercepts I_{11} and I_{33} were obtained before. The error of such an exchange will be small. Assuming $\sigma_{11}^R - \sigma_{33}^R = 0$ the neutron elastic constant (1+ν)/E follows.

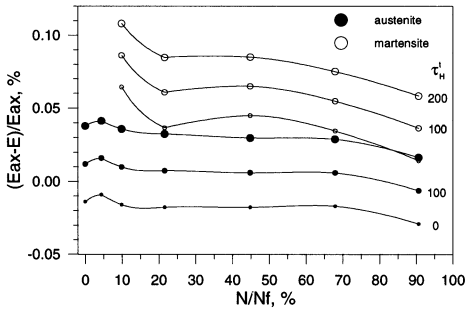

Fig. 28. Variation of the relative difference of $(E_{ax}-E)/E_{ax}$ with the fatigue level at the different values of the hydrostatic residual stress.

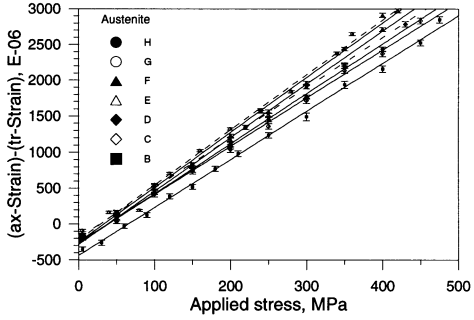

Fig. 29. Difference of elastic strains in the axial and transverse directions vs the applied stress for austenite.

This approach takes advantage of the nominally similar elastic properties of the austenite and martensite, allowing equal partitioning of the applied stress. Results of the calculations of the difference of the elastic strains in the axial and transverse directions for the austenite and the martensite are presented in Figs. 29-30. From the slope of the linear fit of the elastic part of the difference we can obtain the dependence of E/(1+ν) on the fatigue level for the austenite and the martensite shown in Fig. 31.

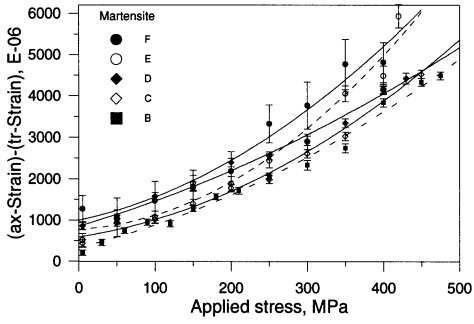

Fig. 30. Difference of elastic strains in the axial and transverse directions vs the applied stress for martensite.

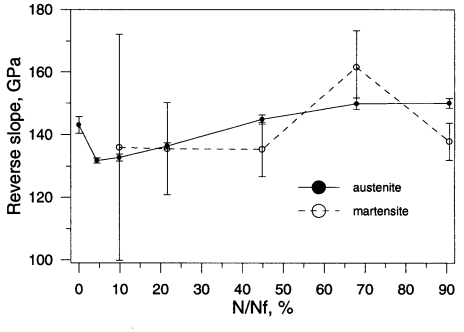

Fig. 31. Parameter of E/(1+ν) (phase reverse slope) vs the fatigue level.

Note that: 1) for both phases, the values of E/(1+ν) obtained using this approach nearly coincide with the "quasielastic" constants obtained before; 2) there is no correlation between the martensite value of E/(1+ν) and the structural transformation of the martensite phase from the needle like shape to the block form with higher volume fraction; 3) once again a clear trend in the value of the austenite constant can be seen, with a clear increase as a function of fatigue level.

5.2. Reuss or Voigt model? In section 5.1 we have calculated the phase strains using the averaged value of $(I_{11}+I_{33})/2$ with the intercepts I_{11} and I_{33} (see Eqs. (A28-A29)) instead a stress-free reference lattice parameter a_0. Now we use the results of the calculation of the total phase strains to estimate the total stresses in the axial direction by help of Hooke's law:

$$\sigma_{11}^{t} = \frac{E}{1+\nu}[\varepsilon_{11} - \frac{\nu}{1-2\nu} Tr(\varepsilon_{ij})]. \quad (4)$$

The results of the calculation of the total phase stresses in both phases for sample B are shown in Fig. 33. For better readability of the figure, the austenite and martensite curves are shifted down and up, respectively.

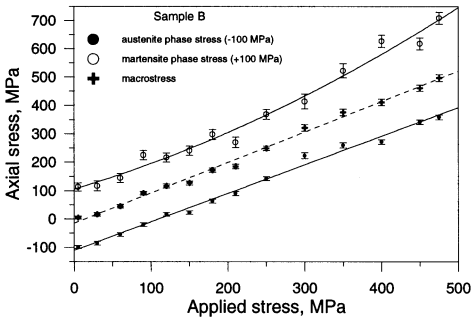

Fig. 33. Phase stresses and macrostresses in the axial direction vs the applied stress for the sample B.

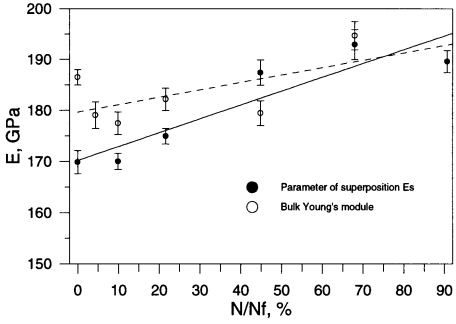

Fig. 34. Parameter of a superposition of $E_{ax,aus}(1-f)+E_{ax,mar}f$ vs the fatigue level as well as the bulk Young's module.

From the experimental data presented in Fig. 33 we might hope to obtain some information about the coupling conditions of the phases in the samples using an approach described in [11], however since the elastic constants of the phases are so similar, there is unlikely to be much separation between different models of elastic behaviour. According to Reuss's model [12] the loading stress must be homogeneously distributed in the both phases. Consequently, the slopes ${}^{i}s_{11}$ of the i-phase stress dependencies in Fig. 33 should be equal and their ratio is giving by

$$R_{Reuss} = \frac{{}^{m}s_{11}}{{}^{a}s_{11}} = 1. \quad (5)$$

In Voigt's model [13] the strains due to loading are homogeneous in both phases and the ratio of the slopes should be equal

$$R_{Voigt} = \frac{{}^{m}s_{11}}{{}^{a}s_{11}} = \frac{{}^{m}E/({}^{m}\nu+1)}{{}^{a}E/({}^{a}\nu+1)} \quad (6)$$

that gives R_{Voigt}=0.92(5) using the "quasielastic" constants for the sample B from Figs. 10-11. The experimental ratio $R_{measured}$ of the martensite and austenite slopes for the sample B is equal 1.00(8). Hence the proximity of all three ratios R_{Reuss}, R_{Voigt} and $R_{measured}$ does not permit separation of models for the coupling conditions of the phases. The measurement accuracy with other samples was worse than the values given for sample B due to the lower martensite fraction, and the subsequent reduced statistical precision of the martensite phase measurement.

5.3. Principle of a superposition of the elastic constants. Given the weak dependence of this material on the coupling model used, we may state that from the principle of superposition, the Young's modulus E_s of the two phase system should approximately follow the equation

$$E_s = E_{aus}(1-f) + E_{mar} f \,. \tag{7}$$

The data in Fig. 34 gives a linear dependence of the summed modulus as a function of fatigue level. In the same figure we show the bulk Young's modulus from Table 1 that was measured after the neutron experiments. Though appreciable distinction between two data sets is visible the tendency for an increase in the Young's module is clearly seen in both cases.

5.4. Macrostresses and microstresses induced by the applied stress. Using the results of the calculation of the total phase stresses in both phases for sample B shown in Fig. 33 and well-known formula for the macrostress

$$\sigma_{11}^{M} = {}^{a}\sigma_{11}^{t}(1-f) + {}^{m}\sigma_{11}^{t} f \tag{8}$$

where the phase index 'a' and 'm' designates austenite and martensite, respectively, we have calculated the dependence of the macrostress on the applied stress (Fig. 33, middle curve). Though the macrostress dependence is the superposition of the linear (austenite) and nonlinear (martensite) curves the resulting curve is very close to the linear dependence, due to the small martensite volume fraction. The dependence is more clear in Fig. 35 where the applied stress is deducted the macrostresses as well as from the total phase stresses. Note that we would expect the 'macrostress' results in Fig. 35 to be zero and constant if the neutron gauge covered a full cross section of the sample.

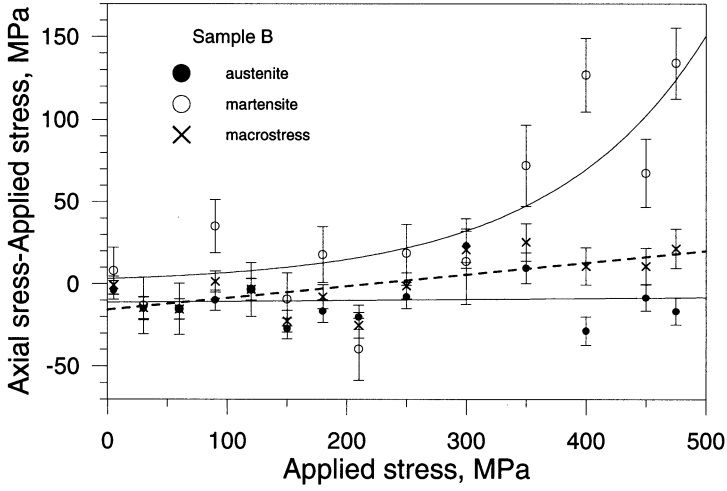

Fig. 35. Differences of the phase stresses and the macrostresses and the applied stress vs the applied stress for the sample B.

Considering the microstresses, the results in Fig. 35 show that the applied stress does not induce additional microstresses in the austenite phase compared to those due to fatigue, whereas appreciable microstresses are induced in the martensite phase in the plastic region. These microstresses are the most likely explanation for the nonlinear behaviour of the martensite phase elastic response in the plastic region under loading. A more detailed understanding of this problem will require additional microstructural examination for damage, texture and martensite grain shape before definitive conclusions can be drawn, since they are unlikely to be due to plastic misfit alone.

6. Conclusions

The main results of this study are:

- The application of the time-of-flight neutron diffraction to separate the individual responses of phases in multiphase materials is demonstrated on the example of a fatigued austenitic stainless steel AISI 321.
- Samples were cycled by the uniaxial tensile-compressive loading under total-strain control with an amplitude of 1% at a frequency of 0.5 Hz. As plastic deformation occurs during fatigue the martensite fraction increases. The samples were subsequently measured using the *in situ* stress rig under tensile stress control on the ENGIN instrument. The Rietveld and Le Bail refinements within the GSAS code were applied to process collected neutron diffraction spectra.
- The applied stress - elastic strain responses of austenite matrix and martensite volume areas were determined for both axial and transverse directions relatively the load axis. An unusual phenomenon is observed: nonlinear behaviour of martensite elastic response in the plastic region, while the austenite elastic response remains linear throughout the measured stress range.
- The effect of residual stress on observed diffraction elastic constants was described but found to be small. The neutron diffraction elastic constants in both phases were calculated from the experimental data and found to be similar. Comparison with the results from mechanical testing was made. The elastic constants generally increased with increasing fatigue level.
- The deviatoric residual microstresses in all the samples were separated into austenite and martensite contributions. The austenite microstress is tensile in the axial direction and compressive in the transverse direction. At the same time the martensite microstresses in the same directions have the opposite sign with magnitudes larger than in the austenite matrix in accordance with the smaller volume fraction. The large martensite microstress could lead to crack initiation that it was found in sample B (90 % fracture fatigue level).
- Inhomogeneous distributions of the loading stresses in the austenite and martensite phases were observed during the tensile experiment. The applied stress does not induce additional microstresses in the austenite phase, however appreciable microstresses are induced in the martensite phase in the plastic region, providing the most likely mechanism for the unusual strain response of the phases. It will require additional microstructural examination of damage, texture and martensite grain shape before conclusions can be drawn as to the cause of these microstresses.
- The single peak analysis of many reflections of the austenitic and martensitic phases shows that the elastic strains of the both phases linearly vary with the anisotropy factor G up to a stress of 400 - 500 MPa indicating that the measured elastic strains are of type I.
- The modified Le Bail refinement accounting for the elastic anisotropy was used to calculate the anisotropy strains. We have observed a qualitative similarity between the applied stress - anisotropy strain response for austenite and martensite. The Le Bail predicted elastic anisotropy hkl-strains of the both phases agree semi-quantitatively with results of single peak analysis of reflections.

Acknowledgements

One of the authors (Yu.T.) is grateful to the ISIS facility for the allocation of the beam time at the ENGIN instrument in a period of 2000-2001 under the RAL-JINR interlaboratory agreement as well as to Prof. R.A.Winholtz from University of Missouri (USA) for the very useful consultations.

References

[1] G.D.Bokuchava, V.V.Luzin, J.Schreiber, Yu.V.Taran. Textures and Microstructures Vol. 33 (1999), p. 279.

[2] M.R.Daymond, M.A.Bourke, R.B.Von Dreele et al. J.App.Phys. Vol. 82 (1997), p. 1554.

[3] M.W.Johnson, L.Edwards, P.J.Withers. Physica B Vol. 234-236 (1997), p. 1141.

[4] M.R.Daymond, D.Eifler, J.Schreiber, Yu.V.Taran. In: The ISIS Facility Annual Report 2000-2001. RAL-TR-2001-050, Didcot, October 2001, v.2, ISIS Experimental Reports, PEARL report of RB 12023.

[5] M.R.Daymond, H.G.Priesmeyer. Acta Mater. Vol. 50 (2002), p. 1613.

[6] M.W.Johnson, M.R.Daymond. In: Analysis of Residual Stress by Diffraction using Neutron and Synchrotron Radiation. UK: Gordon & Breach Publishing, 2002, *in press.*

[7] L.B.McCusker, R.B.Von Dreele, D.E.Cox et al. J.App.Cryst. Vol. 32 (1999), p. 36.

[8] F.Bollenrath, V.Hauk, E.H.Muller. Z.Metallkunde Vol. 58 (1967), p. 76.

[9] M.R.Daymond, M.W.Johnson. J.Appl.Cryst. Vol. 34 (2001), p. 263.

[10] L.Pintschouvius. In: Measurement of Residual and Applied Stress using Neutron Diffraction. The Netherlands: Klumer Academic Publishers, 1992, p.115.

[11] D.Amos, B.Eigenmann, B.Scholtes et al. In: Proc. 4th Inter. Conf. on Residual Stresses. Bethel (USA): Society for Experimental Mechanics, 1994, p.173.

[12] A.Reuss. Z. fur angew. Math. und Mech. Vol. 9 (1929), p.49.

[13] W.Voigt. Lehrbuch der Kristallphysik. Berlin: Teubner-Verlag, 1928.

Appendix: *Multiphase system under loading*

At first we will discuss stresses only one phase in multiphase system therefore we omit the phase indicated index. The total phase strain $\varepsilon_{\varphi\psi}$ along the neutron scattering vector Q is in terms of the stresses in the sample coordinate system (Fig. 1A) [1A]:

$$\varepsilon_{\varphi\psi} = \frac{1+\nu}{E}(\sigma_{11}\cos^2\varphi + \sigma_{12}\sin 2\varphi + \sigma_{22}\sin^2\varphi - \sigma_{33})\sin^2\psi + \frac{1+\nu}{E}\sigma_{33} - \frac{\nu}{E}Tr(\sigma_{ij}) + \frac{1+\nu}{E}(\sigma_{13}\cos\varphi + \sigma_{23}\sin\varphi)\sin 2\psi \quad \text{(A1)}$$

where the angles φ and ψ correspond the rotation of the laboratory and sample coordinate systems with respect to each other.

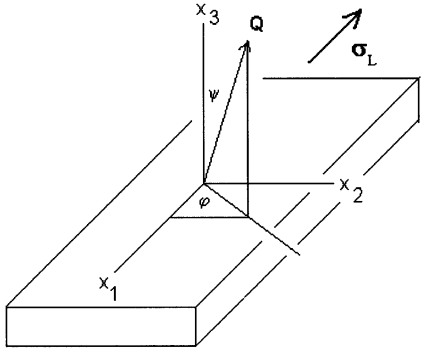

Fig. 1A. Sample coordinate system.

In our measurements a sample had a cylindrical form and an applied stress was uniaxial along the sample axis which we are noted as the x_1 direction. Assuming that all the sample coordinate system axes are principal we have obtained the axial, hoop (tangential) and radial (normal) components of the strain, respectively:

$$\varepsilon_{11} = \frac{1+\nu}{E}\sigma_{11} - \frac{\nu}{E}Tr(\sigma_{ij}),$$
$$\varepsilon_{22} = \frac{1+\nu}{E}\sigma_{22} - \frac{\nu}{E}Tr(\sigma_{ij}), \quad \text{(A2)}$$
$$\varepsilon_{33} = \frac{1+\nu}{E}\sigma_{33} - \frac{\nu}{E}Tr(\sigma_{ij}).$$

Here σ_{ij} is the total phase stress tensor which includes the applied stress σ_{ij}^L, the phase residual stresses σ_{ij}^R and the phase microstresses σ_{ij}^m induced by the applied stress due to the elastic incompatibility (mismatch) of the phases

$$\sigma_{ij}^m = S_{ijkl}\sigma_{kl}^L \quad \text{(A3)}$$

where S_{ijkl} is the fourth rank tensor which depends on the phase morphology. All components of the tensor σ_{ij}^m can be expressed through the applied stress σ_L with different coefficients before it which we are noted as B_{ij}:

$$\sigma_{ij}^m = B_{ij}\sigma_L. \quad \text{(A4)}$$

Separating σ_{ij} on constituents we have

$$\varepsilon_{11} = \frac{\sigma_L}{E}[1 + (1+\nu)B_{11} - \nu Tr(B_{ij})] + \frac{1+\nu}{E}\sigma_{11}^R - \frac{\nu}{E}Tr(\sigma_{ij}^R),$$
$$\varepsilon_{22} = \frac{\sigma_L}{E}[-\nu + (1+\nu)B_{22} - \nu Tr(B_{ij})] + \frac{1+\nu}{E}\sigma_{22}^R - \frac{\nu}{E}Tr(\sigma_{ij}^R) \quad \text{(A5)}$$
$$\varepsilon_{33} = \frac{\sigma_L}{E}[-\nu + (1+\nu)B_{33} - \nu Tr(B_{ij})] + \frac{1+\nu}{E}\sigma_{33}^R - \frac{\nu}{E}Tr(\sigma_{ij}^R).$$

During our neutron experiment we have measured the lattice parameters a_{11} along the axial direction and a_{tr} along the transverse direction vs σ_L. First of three equations (A5) can be written in the a_{ii}-presentation:

$$a_{11} = \frac{a_0\sigma_L}{E}[1+(1+\nu)B_{11} - \nu Tr(B_{ij})] + [\frac{1+\nu}{E}\sigma_{11}^R - \frac{\nu}{E}Tr(\sigma_{ij}^R) + 1]a_0. \qquad \text{(A6-1)}$$

where a_0 is the stress-free value of the lattice parameter. The lattice parameter a_{tr} reflects a combination of the hoop and radial components of the strain. In order to not complicate a calculation we ignore the hoop component. Then the transverse strain gains a sense of the normal component and we can write:

$$a_{33} = \frac{a_0\sigma_L}{E}[-\nu+(1+\nu)B_{33} - \nu Tr(B_{ij})] + [\frac{1+\nu}{E}\sigma_{33}^R - \frac{\nu}{E}Tr(\sigma_{ij}^R) + 1]a_0. \qquad \text{(A6-2)}$$

In Figs. 2A and 3A we have presented schematically both curves $a_{11}(\sigma_L)$ and $a_{33}(\sigma_L)$.

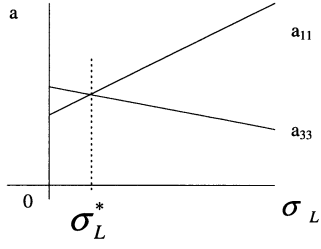

Fig. 2A. $\sigma_{11}^R > \sigma_{33}^R$.

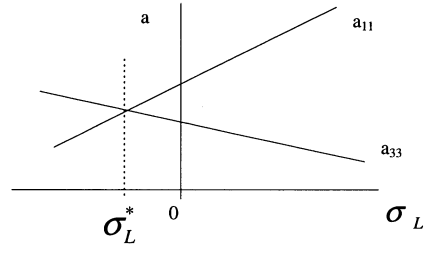

Fig. 3A. $\sigma_{11}^R < \sigma_{33}^R$.

From the linear fits of the experimental data it is possible to obtain the intercepts I_{11} and I_{33}, the slopes S_{11} and S_{33}, the intersection σ_L^*. To calculate these values we will be considered the single and two phase systems, in turn.

The single phase system. In our case this corresponds to sample H - the noncycled pure austenite. Then we obtain

$$\begin{aligned} a_{11} &= \frac{a_0\sigma_L}{E} + [\frac{1+\nu}{E}\sigma_{11}^R - \frac{\nu}{E}Tr(\sigma_{ij}^R) + 1]a_0, \\ a_{33} &= -\frac{a_0\nu\sigma_L}{E} + [\frac{1+\nu}{E}\sigma_{33}^R - \frac{\nu}{E}Tr(\sigma_{ij}^R) + 1]a_0 \end{aligned} \qquad \text{(A7)}$$

The intercepts I_{11} and I_{33}, the slopes S_{11} and S_{33}, the intersection σ_L^* are giving by

$$I_{11} = [\frac{1+\nu}{E}\sigma_{11}^R - \frac{\nu}{E}Tr(\sigma_{ij}^R) + 1]a_0, \qquad \text{(A8)}$$

$$I_{33} = [\frac{1+\nu}{E}\sigma_{33}^R - \frac{\nu}{E}Tr(\sigma_{ij}^R) + 1]a_0, \qquad \text{(A9)}$$

$$S_{11} = \frac{a_0}{E}, \qquad \text{(A10)}$$

$$S_{33} = -\frac{a_0\nu}{E}, \qquad \text{(A11)}$$

$$\sigma_L^* = -\frac{I_{11} - I_{33}}{S_{11} - S_{33}} = -(\sigma_{11}^R - \sigma_{33}^R). \qquad \text{(A12)}$$

Note that the ratio of slopes is

$$\frac{S_{33}}{S_{11}} = -\nu . \tag{A13}$$

Thus, in the case of the single phase system Poisson's ratio may be exactly determined from the linear fits of the experimental curves $a_{11}(\sigma_L)$ and $a_{33}(\sigma_L)$ even if the residual stresses are present in the sample. We introduce the "quasielastic" constants E_{ax} and E_{tr} in the axial and transverse direction, respectively:

$$\begin{aligned} E_{ax} &= \frac{I_{11}}{S_{11}} = (1+\nu)\sigma_{11}^R - \nu Tr(\sigma_{ij}^R) + E, \\ E_{tr} &= \frac{I_{33}}{S_{33}} = -\frac{1}{\nu}[(1+\nu)\sigma_{33}^R - \nu Tr(\sigma_{ij}^R) + E]. \end{aligned} \tag{A14}$$

Only in the absence of the residual stresses the "quasielastic" constants turn into the true elastic constants E and -E/ν.

From the five equations (A8-A12) we have only four independent equations with the five unknowns E, ν, a_0, σ_{11}^R and σ_{33}^R. To restore the residual stress tensor an accurate value of a_0 must be available. In our case this is not so. This problem can be resolved [2A] if we are interesting only a change of the residual stresses during any process, by separating the residual stress tensor into the hydrostatic and deviatoric residual stress tensors τ_H^R and τ_{ij}^R, respectively:

$$\sigma_{ij}^R = \delta_{ij}\tau_H^R + \tau_{ij}^R \tag{A15}$$

where the hydrostatic stress is

$$\tau_H = Tr(\sigma_{ij}^R)/3, \tag{A16}$$

at that

$$Tr(\tau_{ij}^R) = 0. \tag{A17}$$

As before ignoring the hoop component we have from Eq.(A17)

$$\tau_{33}^R = -\tau_{11}^R. \tag{A18}$$

Then we obtain from Eqs.(A12), (A15) and (A18)

$$\begin{aligned} \tau_{11}^R &= -\frac{1}{2}\sigma_L^*, \\ \tau_{33}^R &= \frac{1}{2}\sigma_L^*. \end{aligned} \tag{A19}$$

The two phase system. The intercepts I_{11} and I_{33}, the slopes S_{11} and S_{33}, the intersection σ_L^* for each phase are giving by (note once more that we omit the phase indicated index)

$$I_{11} = [\frac{1+\nu}{E}\sigma_{11}^R - \frac{\nu}{E}Tr(\sigma_{ij}^R) + 1]a_0, \tag{A21}$$

$$I_{33} = [\frac{1+\nu}{E}\sigma_{33}^R - \frac{\nu}{E}Tr(\sigma_{ij}^R) + 1]a_0, \tag{A22}$$

$$S_{11} = \frac{a_0}{E}[1 + (1+\nu)B_{11} - \nu Tr(B_{ij})], \tag{A23}$$

$$S_{33} = \frac{a_0}{E}[-\nu + (1+\nu)B_{33} - \nu Tr(B_{ij})], \tag{A24}$$

$$\sigma_L^* = -\frac{\sigma_{11}^R - \sigma_{33}^R}{1 + (B_{11} - B_{33})}. \tag{A25}$$

Note that the phase ratio of slopes is

$$\frac{S_{33}}{S_{11}} = \frac{-\nu + (1+\nu)B_{33} - \nu Tr(B_{ij})}{1 + (1+\nu)B_{11} - \nu Tr(B_{ij})} \tag{A26}$$

and it depends only on the phase morphology. The "quasielastic" constants E_{ax} and E_{tr} in the axial and transverse direction, respectively, are:

$$\begin{aligned} E_{ax} &= \frac{I_{11}}{S_{11}} = \frac{(1+\nu)\sigma_{11}^R - \nu Tr(\sigma_{ij}^R) + E}{1 + (1+\nu)B_{11} - \nu Tr(B_{ij})}, \\ E_{tr} &= \frac{I_{33}}{S_{33}} = \frac{(1+\nu)\sigma_{33}^R - \nu Tr(\sigma_{ij}^R) + E}{-\nu + (1+\nu)B_{33} - \nu Tr(B_{ij})}. \end{aligned} \tag{A27}$$

Separating the stress tensor σ_{ij}^R into the hydrostatic and deviatoric tensors and substituting the results into Eqs.(A21-A25) we obtain

$$I_{11} = (\frac{1-2\nu}{E}\tau_H^R + \frac{1+\nu}{E}\tau_{11}^R + 1)a_0, \tag{A28}$$

$$I_{33} = (\frac{1-2\nu}{E}\tau_H^R + \frac{1+\nu}{E}\tau_{33}^R + 1)a_0, \tag{A29}$$

$$S_{11} = \frac{a_0}{E}[1 + (1+\nu)B_{11} - \nu Tr(B_{ij})], \tag{A30}$$

$$S_{33} = \frac{a_0}{E}[-\nu + (1+\nu)B_{33} - \nu Tr(B_{ij})], \tag{A31}$$

$$\sigma_L^* = -\frac{\tau_{11}^R - \tau_{33}^R}{1 + (B_{11} - B_{33})}. \tag{A32}$$

From the five equations (A28-A32) we have only four independent equations with the six unknowns E, ν, a_0, τ_H^R, τ_{11}^R, τ_{33}^R assuming that B_{11}, B_{33} and $Tr(B_{ij})$ can be calculated [3A] if the phase morphology is known. Using Eq.(A17) we obtain

$$\tau_{33}^R = -\tau_{11}^R. \tag{A33}$$

Then we obtain from Eqs.(A32-A33):

$$\begin{aligned} \tau_{11}^R &= -\frac{1}{2}\sigma_L^*[1 + (B_{11} - B_{33})], \\ \tau_{33}^R &= \frac{1}{2}\sigma_L^*[1 + (B_{11} - B_{33})]. \end{aligned} \tag{A34}$$

The stress equilibrium into the two phase system. Using the results of [2A, 4A] we have the deviatoric values of the macrostress τ_{ii}^M and the microstress τ_{ii}^μ in each phase in terms of τ_{ii}^R:

$$\begin{aligned} \tau_{ii}^M &= {}^a\tau_{ii}^R(1-f) + {}^m\tau_{ii}^R f, \\ {}^a\tau_{ii}^\mu &= ({}^a\tau_{ii}^R - {}^m\tau_{ii}^R)f, \\ {}^m\tau_{ii}^\mu &= -({}^a\tau_{ii}^R - {}^m\tau_{ii}^R)(1-f) \end{aligned} \tag{A35}$$

where we have introduces the phase index 'a' and 'm' of austenite and martensite, respectively. Note that the macrostress τ_{ii}^M is the same in each phase.

Accordingly [4A] if gradients of the macrostresses on the sample surface are zero, equilibrium relations require that the normal macrostress component

$$\sigma_{33}^{M} = \tau_{H}^{M} + \tau_{33}^{M} = 0 \tag{A36}$$

at all depths in the material. Then we can calculate the hydrostatic macrostress:

$$\tau_{H}^{M} = -\tau_{33}^{M}. \tag{A37}$$

Thus, the full residual macrostress tensor can be restored:

$$\sigma_{ij}^{M} = \delta_{ij}\tau_{H}^{M} + \tau_{ij}^{M}. \tag{A38}$$

Really, only the axial component is not zero:

$$\sigma_{11}^{M} = \tau_{H}^{M} + \tau_{11}^{M} = \tau_{11}^{M} - \tau_{33}^{M}. \tag{A39}$$

References of Appendix

[1A] I.C.Noyan, J.B.Cohen. Residual Stresses (Measurement by Diffraction and Interpretation). New York: Springer-Verlag, 1987.

[2A] R.A.Winholtz, J.B.Cohen. Adv. in X-ray Analysis Vol. 32 (1989), p. 341.

[3A] T.Mura. Micromechanics of Defects in Solids. The Netherlands: Martinus Nijhoff Publishers, 1982.

[4A] I.C.Noyan. Met. Trans. Vol. 14A (1983), p. 1907.

Received on July 7, 2002.

Таран Ю. В. и др. E14-2002-161

Исследование с помощью нейтронного стресс-анализа механических свойств образцов из метастабильной аустенитной стали AISI 321, подвергнутых низкочастотному усталостному циклированию, в зависимости от внешней нагрузки

Упругие и пластические свойства аустенитной матрицы и мартенситных включений, индуцированных в низкоуглеродистой метастабильной аустенитной нержавеющей стали во время циклического нагружения типа «растяжение–сжатие», исследованы в *in situ* нейтрон-дифракционном эксперименте с нагрузочной машиной на установке ENGIN на импульсном источнике нейтронов ISIS. Образцы были изготовлены из стали AISI 321, отожженной при температуре 1050 °C и закаленной в воде. Они были подвергнуты низкочастотному (0,5 Гц) усталостному циклированию с амплитудой деформации 1 %. В результате обработки нейтрон-дифракционных спектров методами Ритвельда и Ле Бэйла получены кривые деформации аустенитной и мартенситной фаз, из которых определены упругие постоянные обеих фаз в зависимости от степени усталости. Также представлены результаты обработки, учитывающей упругую анизотропию в поликристаллическом материале под нагрузкой. Остаточная деформация в аустенитной матрице определена с использованием нециклированного образца как эталона. Остаточные макронапряжения и сдвиговые компоненты фазовых остаточных микронапряжений определены в предположении близости упругих свойств обеих фаз.

Работа выполнена в Лаборатории нейтронной физики им. И. М. Франка ОИЯИ.

Сообщение Объединенного института ядерных исследований. Дубна, 2002

Taran Yu. V. et al. E14-2002-161

Study of Mechanical Features for Low Cycle Fatigue Samples of Metastable Austenitic Steel AISI 321 by Neutron Stress Analysis under Applied Load

The elastoplastic properties of the austenitic matrix and martensitic volume areas induced during cyclic tensile-compressive loading of low carbon metastable austenitic stainless steel were studied in an *in situ* neutron diffraction stress rig experiment on the ENGIN instrument at the ISIS pulsed neutron facility. Samples prepared from the steel AISI 321 annealed at 1050 °C and quenched in water were subjected to low-cycle fatigue under total-strain control with an amplitude of 1 % at a frequency of 0.5 Hz. Subsequent applied stress–elastic strain responses of the austenitic and martensitic phases were obtained by Rietveld and Le Bail refinements of the neutron diffraction spectra, and were used to determine the elastic constants of the phases as a function of fatigue level. The results of modified refinements accounting for the elastic anisotropy in polycrystalline materials under load are also presented. The residual strains in the austenitic matrix were determined as a function of fatigue cycling, using a noncycled sample as a reference sample. The residual macrostresses and the deviatoric components of the phase residual microstresses were determined assuming that the elastic properties of both phases are similar.

The investigation has been performed at the Frank Laboratory of Neutron Physics, JINR.

Communication of the Joint Institute for Nuclear Research. Dubna, 2002

Макет *Т. Е. Попеко*

ЛР № 020579 от 23.06.97.
Подписано в печать 24.07.2002.
Формат 60 × 90/16. Бумага офсетная. Печать офсетная.
Усл. печ. л. 1,68. Уч.-изд. л. 2,82. Тираж 290 экз. Заказ № 53444.

Издательский отдел Объединенного института ядерных исследований
141980, г. Дубна, Московская обл., ул. Жолио-Кюри, 6.